Editors' Suggestion

Probing the edge states of Chern insulators using microwave impedance microscopy

Taige Wang,[1,2,3] Chen Wu,[3] Masataka Mogi,[4] Minoru Kawamura,[5] Yoshinori Tokura,[5,6] Zhi-Xun Shen,[7,8,9] Yi–Zhuang You,[3] and Monica T. Allen[3]

[1]*Department of Physics, University of California, Berkeley, California 94720, USA*
[2]*Material Science Division, Lawrence Berkeley National Laboratory, Berkeley, California 94720, USA*
[3]*Department of Physics, University of California, San Diego, California 92093, USA*
[4]*Department of Physics, Massachusetts Institute of Technology, Cambridge, Massachusetts 02139, USA*
[5]*Strong Correlation Physics Research Group, RIKEN Center for Emergent Matter Science, Saitama 351-0198, Japan*
[6]*Department of Applied Physics and Tokyo College, University of Tokyo, Tokyo 113-8654, Japan*
[7]*Department of Applied Physics, Stanford University, Stanford, California 94305, USA*
[8]*Geballe Laboratory for Advanced Materials, Stanford University, Stanford, California 94305, USA*
[9]*Stanford Institute for Materials and Energy Sciences, Stanford Linear Accelerator Center National Accelerator Laboratory, Menlo Park, California 94025, USA*

(Received 15 July 2023; accepted 8 December 2023; published 29 December 2023)

Microwave impedance microscopy (MIM) has been utilized to directly visualize topological edge states in many quantum materials. While the microwave response for conventional metals and insulators can be accurately quantified using simple lumped-element circuits, whose applicability to more exotic quantum systems remain limited. In this work, we present a general theoretical framework of the MIM response of arbitrary quantum materials. Applying it to topological edge states in a Chern insulator predicts an enhanced MIM response at the crystal boundaries due to collective edge magnetoplasmon (EMP) excitations. The unique resonance frequency of these plasmonic modes allows one to disentangle the signatures of topological versus trivial edge states. To benchmark our analytical predictions, we experimentally probe the MIM response of quantum anomalous Hall edge states in a Cr-doped $(Bi, Sb)_2Te_3$ topological insulator and perform numerical simulations using a classical formulation of the EMP modes based on this realistic tip-sample geometry, both of which yield results consistent with our theoretical picture. We also show how the technique of MIM can be used to quantitatively extract the topological invariant of a Chern insulator and shed light on the microscopic nature of dissipation along the crystal boundaries.

DOI: 10.1103/PhysRevB.108.235432

I. INTRODUCTION

Chern insulators host chiral one-dimensional edge states and exhibit a quantized Hall conductance due to a nontrivial topological band structure. The experimental signatures of Chern insulators have been observed in a variety of material systems, from the quantum Hall family to magnetic topological insulators, and more recently moiré materials [1–10]. A key feature of Chern insulators is the presence of topological edge modes, which are electronic states that propagate unidirectionally along the edges of the material without backscattering. While edge states in Chern insulators have been investigated extensively using electronic transport techniques [11–14], these methods lack the spatial resolution to probe the detailed structure and the degree of localization of these modes.

To address this limitation, several imaging techniques have been used to directly visualize topological edge modes, including scanning tunneling microscopy (STM) [15–19], superconducting quantum interference device (SQUID) microscopy [20–22], as well as some interferometry techniques [23]. These experiments have detected current flow and an enhancement of the density of states at the boundaries of topological insulators, which have been interpreted as evidence for one-dimensional topological edge modes. However, this interpretation can be complicated by the presence of trivial electronic states at the physical boundaries arising from impurities, dangling bonds, and band bending [24–26].

In recent years, a near-field imaging technique called scanning microwave impedance microscopy (MIM) has shown great potential for spatially resolved detection of topological boundary modes. Experiments have reported an enhanced microwave response at the edges of two-dimensional topological insulators and quantum Hall systems [24,27–31], but the observed behavior cannot be easily explained by a simple conductance increase close to the edge using classical lumped-circuit models. Furthermore, the observed width of quantum Hall edge states, as measured by MIM, is an order of magnitude larger than that measured by transport techniques and STM, significantly exceeding the magnetic length [15–19,32–36]. This motivates our development of a theoretical foundation to compute the microwave response of quantum materials that cannot simply be characterized by a scalar conductivity value.

In this paper, we develop a general theoretical framework that quantifies the MIM response of a quantum material within linear response theory. Upon applying this theory to the special case of quantum anomalous Hall (QAH) insulators, we predict that an enhanced MIM response at the edge should arise from collective edge magnetoplasmon (EMP) modes that circulate along the sample boundary [37–44]. The resonance frequency of these plasmonic modes should depend quantitatively on the topological invariant of the Chern insulator state and on the length of the sample's perimeter [37–40]. This nontrivial frequency dependence can unambiguously relate the enhanced edge signal observed with MIM to the one-dimensional topological edge modes that propagate around the entire sample perimeter, whereas topologically trivial edge effects are expected to be featureless in the frequency domain.

To check the validity of this analytical model, we experimentally measured the real-space MIM response of the QAH edge modes in a Cr-doped $(Bi, Sb)_2Te_3$ magnetic topological insulator at various microwave frequencies and also conducted numerical simulations based on this experimental tip-sample setup, both of which yielded results consistent with the theoretical framework proposed here.

II. THEORY OF THE MIM RESPONSE OF QUANTUM MATERIALS

MIM characterizes a material's electronic response to microwave frequency electromagnetic fields confined to a small spatial region around a sharp metallic probe. In practice, a microwave excitation is coupled to an atomic force microscopy (AFM) tip in close proximity to the sample, and the real and imaginary parts of the reflected signals are measured using gighertz lock-in detection techniques [45–47].

We first review the basics of the MIM measurement setup and then present a general model of the MIM response of quantum materials within linear response theory. As shown in Fig. 1, the MIM probe, driven by an AC voltage at microwave frequency, is brought near the sample surface. Unlike STM, the probe is only capacitively coupled to the sample. MIM measures the displacement current exchanged between the probe and the sample. This displacement current I can be formally written as $I = Y_{ts}V$, where V is the driven voltage and Y_{ts} is the complex tip-sample admittance [45].

In practice, an impedance matching network is always necessary to maximize the sensitivity of the admittance measurement. Since Y_{ts} is much smaller than the self-admittance of the MIM probe Y_t, the MIM signals are linearly proportional to the change in Y_{ts}. Explicitly [45],

$$\mathrm{Re\,MIM} + i\mathrm{Im\,MIM} \approx a(\mathrm{Re}\,Y_{ts} + i\mathrm{Im}\,Y_{ts}) + b, \tag{1}$$

where a is a real constant and b is a complex constant. In the following section, we show how to obtain Y_{ts} in terms of the density response function of the system.

A. General framework

The most commonly used model of Y_{ts} is the lumped-element model, which treats the sample as a resistor and a capacitor in parallel, then coupled capacitively to the tip [47]. This model can accurately predict the MIM response of conventional metals, dielectrics, and certain two-dimensional materials [46]. However, a more general theoretical framework is required to properly quantify the microwave response of more complex quantum materials, such as topological states of matter, that cannot be simply described by a pair of scalar conductivity and permittivity values. For example, in the case of QAH insulators, the model must accommodate one-dimensional gapless plasmon modes at the sample edge, which is outside the scope of the traditional lumped element picture.

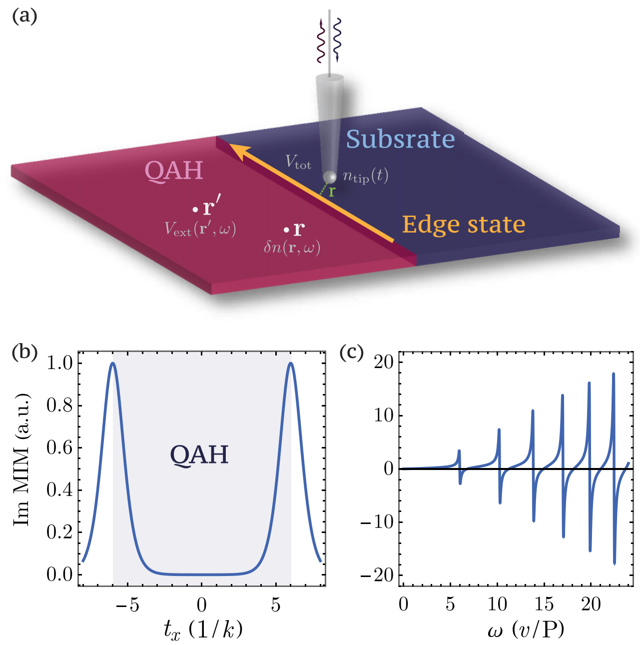

FIG. 1. Theoretical MIM response of topological edge modes in a quantum anomalous Hall insulator. (a) Schematic illustration of the measurement setup, in which the MIM probe is scanned across the QAH insulator edge. The probe is driven by an AC voltage at microwave frequencies and then the displacement current is measured. The MIM signal can be computed by convolving with the correlation function $\chi(\boldsymbol{r}, \boldsymbol{r}')$ inside the sample. (b), (c) The imaginary part of the MIM response of a QAH insulator according to Eq. (9). In panel (b), the tip is scanned across the sample at fixed frequency ω and the sample lies within the shaded region (between $x = \pm 6/k_\omega$). Here t_x is the tip location in units of $1/k_\omega$, with k_ω being the EMP momentum defined by $\omega \sim \omega_{\rm EMP}(k_\omega)$. In panel (c), the tip is situated over the sample edge ($r = d$) while the frequency ω is swept. We used $d = 0.005P$, $l = 0.2P$, and $e^2/[(2\pi)^2\epsilon_0] = 0.2\hbar v$, where v is the edge velocity and P is the sample perimeter. In both cases, parameters are chosen to be relevant to the numerical simulation.

We start by considering a tip at $\boldsymbol{r}_t$, which generates an external potential $V_{\rm ext}(\boldsymbol{r}, t) = G(\boldsymbol{r}, \boldsymbol{r}_t)Q_t(t)$ on the sample, where $Q_t(t)$ is the external charge at the apex of the tip, and $G(\boldsymbol{r}, \boldsymbol{r}')$ is the Coulomb interaction inside the dielectric environment. We note that the geometry of the tip can be completely captured by $G(\boldsymbol{r}, \boldsymbol{r}')$, which can either be calculated numerically or be approximated by the vacuum value of a single tip apex, $G(\boldsymbol{r}, \boldsymbol{r}') \approx 1/4\pi\epsilon_0|\boldsymbol{r} - \boldsymbol{r}'|$. Now we write down the induced charge density in the sample in terms of the density response function,

$$\delta n(\boldsymbol{r}, \omega) = e\int d\boldsymbol{r}'\chi(\boldsymbol{r}, \boldsymbol{r}'; \omega)V_{\rm ext}(\boldsymbol{r}', \omega), \tag{2}$$

with $\boldsymbol{r}$ and $\boldsymbol{r}'$ both inside the sample. We drop the index ω below to simplify the notation. This induced charge density in turn generates a potential $V_t = -e\int d\boldsymbol{r} G(\boldsymbol{r}_t, \boldsymbol{r})\delta n(\boldsymbol{r})$ at the apex of tip. The total potential at the peak of the tip has an additional term due to the tip head capacitance C_t, $V_{\text{tot}} = Q_t/C_t + V_t$, then we can find the tip-sample admittance by expanding $Y_{\text{tot}} = \partial_t Q_t(t)/V_{\text{tot}}$ to the leading order in $C_t V_t/Q_t$,

$$Y_{\text{ts}} \approx -i\omega e^2 C_t^2 \int d\boldsymbol{r} d\boldsymbol{r}' G(\boldsymbol{r}_t, \boldsymbol{r})\chi(\boldsymbol{r}, \boldsymbol{r}')G(\boldsymbol{r}', \boldsymbol{r}_t). \tag{3}$$

We note that all constant terms and prefactors will be absorbed in the constants a and b in Eq. (1) during impedance matching and therefore they are neglected from now on. Equation (3) is one of the main results of this work, which characterizes the MIM response of arbitrary quantum systems with $\chi(\boldsymbol{r}, \boldsymbol{r}')$ describing the dynamical charge density-density correlation between $\boldsymbol{r}$ and $\boldsymbol{r}'$ in the sample. The derivation of this equation uses only two assumptions: the tip can be approximated by a single point, and the microwave frequency electromagnetic field generated by MIM can be treated within linear response theory. The first assumption is verified in a special case through numerical simulations in Sec. III, while the second assumption is supported by the high sensitivity of MIM provided by impedance matching.

Before we proceed to apply this general framework to Chern insulators, we will make a few comments on the result presented in Eq. (3). First, this general result reduces to the lumped element model in the case of a simple homogeneous metal sheet with dielectric function $\epsilon(\boldsymbol{q})$,

$$\chi(\boldsymbol{q}) = \frac{\epsilon_0^2}{e^2}\left(\frac{1}{\epsilon_0} - \frac{1}{\epsilon(\boldsymbol{q})}\right)|\boldsymbol{q}|^2,$$
$$Y_{\text{ts}} \sim -i\omega \frac{1}{32\pi}\frac{t^2}{d^2}\left(\frac{1}{\epsilon_0} - \frac{1}{\epsilon_{\text{eff}}}\right), \tag{4}$$

where t is the sample thickness, d is the tip-sample distance, and ϵ_{eff} is the effective dielectric constant. ϵ_{eff} approaches the usual DC dielectric constant $\epsilon(\boldsymbol{q} = 0)$ in the limit when the tip is sufficiently far from the sample. The lumped element model parameters are given by the sample resistance $R_s \sim 1/\omega \text{Im}\,\epsilon_{\text{eff}}$ and the sample capacitance $C_s \sim \text{Re}\,\epsilon_{\text{eff}}$. The tip-sample capacitance C_0 only shows up in constant terms and prefactors (see Ref. [47], Sec. SI, for definitions and a full derivation).

Second, in the limit when the tip is sufficiently far from the sample, we can further approximate $\chi(\boldsymbol{q})$ by $\chi(\boldsymbol{q} = 0)$; then the MIM signal can be related to the electronic compressibility $dn/d\mu$ as follows:

$$Y_{\text{ts}} \sim -i\chi(\boldsymbol{q} = 0) = -i\frac{\delta n}{\delta \mu}, \tag{5}$$

where n is the electron density and μ is the chemical potential. This provides a direct correspondence between the imaginary part of the MIM response and the chemical potential $\mu(n)$ (which, for example, can be measured by scanning single-electron transistors and related field penetration techniques [48,49]).

Finally, due to the factor of i in Eq. (3), the imaginary part of the MIM response, $\text{Im}\,Y_{\text{ts}}$, comes from the real part of the density response function, $\text{Re}\,\chi$, and vice versa. Thus, $\text{Im}\,Y_{\text{ts}}$ and $\text{Re}\,Y_{\text{ts}}$ measure the reflectivity and absorption of the sample, respectively.

B. Special case: Application to QAH insulators

To illustrate a concrete example, we now apply this general framework to calculate the MIM response of topological edge modes in a QAH insulator. The recipe is to first find all low-energy excitations, then compute these excitations' contributions to the density response function χ, and finally apply Eq. (3) to find the MIM response. In two-dimensional QAH insulators, the bulk contributes little to the dielectric response because of the large energy gap, so we only need to focus on the edge contribution. The edge states in QAH insulators are characterized by the chiral Luttinger liquid that hosts plasmonic excitations [37,44,50]. These gapless edge plasmon modes are called edge magnetoplasmons (EMP) in the context of quantum Hall insulators and have been studied extensively for several decades [37–39,41–44]. More recently, they have also been studied in the context of QAH insulators [40], quantum spin Hall insulators [51], and Chern insulators [42]. To fully understand EMP modes beyond the chiral Luttinger liquid, prior theory work has also considered semiclassical corrections [37,41–43].

In addition to EMP modes, edge acoustic modes have also been observed in the low-energy excitation spectrum in QAH insulators [52,53]. However, these modes are overdamped at microwave frequencies in the parameter regime of QAH insulators. Therefore, we can safely conclude that the MIM response in QAH insulators is dominated by edge plasmon modes. This is the underlying reason why the MIM response of a QAH insulator behaves so differently from the response of materials in which electron-hole pair excitation dominates. It might be a bit surprising since plasmon modes are usually not expected to show up in MIM data due to their finite energy gap. However, in QAH insulators these EMP modes are gapless due to the one-dimensional (1D) nature of the edge states. In the following, we only focus on the EMP contribution to Y_{ts}.

If we place the tip a linear distance r from the edge, the tip-sample admittance reduces to

$$Y_{\text{ts}} \sim -\frac{i\omega e^2}{P}\sum_k G_r(k)\chi(k)G_r(-k), \tag{6}$$

where k is the 1D momentum along the edge, P is the sample perimeter, and $G_r(k) = K_0(|k|r)/4\pi\epsilon_0$ is the 1D Fourier transform of the Coulomb interaction $1/4\pi\epsilon_0|\boldsymbol{r} - \boldsymbol{r}'|$ with K_0 being the modified Bessel function. In Ref. [47], Sec. SII, we compute $\chi(k)$ for chiral edge modes at the random-phase approximation level,

$$\chi(k) = \frac{1}{2\pi}\frac{k}{\hbar\omega - \hbar v k - \frac{e^2}{(2\pi)^2\epsilon_0}k\log\left(\frac{1}{kl}\right)}, \tag{7}$$

where v is the edge velocity and l is the localization length of the edge mode, which is inversely proportional to the bulk gap and is assumed to be small compared to r in Eq. (6). In pure QAH samples where the Dirac velocity v_F is the only energy scale, we expect $v = v_F$. The poles of $\chi(k)$ define the EMP frequencies,

$$\hbar\omega_{\text{EMP}}(k) = \hbar v k + \frac{e^2}{(2\pi)^2\epsilon_0}k\log\left(\frac{1}{kl}\right). \tag{8}$$

This result agrees with Ref. [37], where the first term is referred to as the quantum part and the second term is referred to as the classical part. The imaginary part of $\chi(k)$ can be obtained by taking $\omega \mapsto \omega + i\epsilon$, then $\mathrm{Im}\chi(k, \omega + i\epsilon) = -k\delta(\hbar\omega - \hbar\omega_{\mathrm{EMP}})/2$, with δ being the delta function. In the experiment, ϵ could be a small but finite number due to dissipation effects, then $\mathrm{Im}\chi(k)$ would become a Lorentzian function centered at $\hbar\omega_{\mathrm{EMP}}$ (see Ref. [47], Sec. SIII A). Therefore, we expect the line shape of the EMP resonance peaks to be broadened in the presence of dissipation along the sample boundaries. These features should allow microwave imaging to shed light on the the microscopic nature of the dissipation in the chiral edge modes, as revealed by the MIM response in the frequency domain.

Since we are operating at microwave frequencies, we have to worry about the quantization of momentum $k = 2\pi n/P$, with n being an integer, given the finite sample diameter P. If the MIM frequency $\omega \sim \omega_{\mathrm{EMP}}(2\pi/P)$ is comparable to the lowest few EMP resonances, the dominant contribution to the MIM response comes from a particular momentum k_ω whose EMP frequency $\omega_{\mathrm{EMP}}(k_\omega)$ is closest to ω, then

$$Y_{\mathrm{ts}} \sim -\frac{i\omega e^2}{32\pi^3\epsilon_0^2 P}\frac{k_\omega}{\hbar\omega - \hbar\omega_{\mathrm{EMP}}(k_\omega)}K_0^2(k_\omega r) \underset{r\to 0}{\sim} -\log^2 k_\omega r. \tag{9}$$

In experiments, we expect the case $\omega \sim \hbar\omega_{\mathrm{EMP}}(2\pi/P)$ to hold given the size of the system [40].

The presence of edge magnetoplasmons should be manifested experimentally in a strong enhancement of the MIM response at the boundaries of the QAH insulator, in agreement with prior experimental results [29,30]. Figure 1(b) shows the spatial profile of the MIM response ($\mathrm{Im\,MIM} \sim \mathrm{Im}Y_{\mathrm{ts}}$) of a QAH edge mode, revealing a sharp peak at the crystal boundaries, following Eq. (9). The width of this edge peak is given by the characteristic length scale $1/k_\omega$, the EMP wavelength, which can be as large as a few microns for realistic sample dimensions. It is generally expected that the edge width measured with MIM will be larger than the actual edge localization length l due to long-range Coulomb coupling between the tip and the sample. This observation helps explain the vastly different edge state widths reported in transport [32,33] and STM [15–19] studies versus MIM experiments [29,30].

Investigating the frequency dependence of the MIM edge peak should shed light on the topological nature of the Chern insulator state. Figure 1(c) illustrates the evolution of the edge peak amplitide as a function of the MIM excitation frequency ω. Here we plot Im MIM as a function of ω for a fixed tip location over the sample edge, with $d = 0.005P$, $l = 0.2P$, and $e^2/[(2\pi)^2\epsilon_0] = 0.2\hbar v$. The EMP resonances appear at a series of discrete microwave frequencies, which are found to depend quantitatively on both the topological invariant and the sample perimeter [37–40]. Because trivial edge states localized at crystal boundaries should be featureless as a function of frequency, this unique fingerprint of the EMP resonances in the frequency domain provides a route to unambiguously differentiate between topological and trivial edge modes. The quantitative relationship between the resonance frequency and the sample circumference also illustrates the nonlocal, topological nature of the chiral edge modes that circulate around the entire sample.

In practice, because continuously sweeping the MIM frequency can be experimentally challenging, one could first identify the EMP resonances using traditional microwave transmission measurements [40] and then perform MIM imagining at a few frequencies close to and away from those EMP resonances.

III. SEMICLASSICAL SIMULATIONS

To verify our analytical results, which were derived using an approximation that treats the MIM tip as a point, we also perform a numerical simulation of the MIM signal that incorporates a realistic tip-sample geometry and dielectric environment that had been neglected in the analytical treatment. The simulation still focuses on the topological edge state contribution to the MIM signal and utilizes a classical formulation of the EMP modes, which accurately captures the density response of these modes even though it may not accurately reproduce the EMP frequencies [41,42]. This formulation requires solving Maxwell's equations with a nonzero Hall conductance inside the sample, which therefore only captures the classical part of the EMP frequencies in Eq. (8).

To compute the admittance Y_{ts}, we use finite element analysis to numerically solve Maxwell's equations for the entire experimental setup, including the MIM tip, the sample, and the substrate, as illustrated schematically in Fig. 2(a) (see Ref. [47], Sec. SIII, for details). The sample is placed on top of the substrate as in the experiment [29], which results in a step across the sample boundary [Fig. 2(a)]. The dielectric environment is set to be identical to the experiment setup, and the conductivity tensor is set to be $\sigma_{xy} = e^2/h$ inside the sample and zero outside. To ensure numerical convergence, we set the sample size to 12 μm × 20 μm, which is much smaller than the one used in the experiment in Ref. [29] and Sec. IV. A side effect of scaling down the sample dimension is that we need to look at much higher frequencies in order to compare with the experiment since the first few EMP frequencies $\omega_n \sim \hbar\omega_{\mathrm{EMP}}(2\pi n/P)$ are scaled up at the same time [see Eq. (8) and Ref. [47] Sec. SIII B for details]. More quantitatively, the first few EMP frequencies are about 13 times larger than one would expect in the sample to be discussed in Sec. IV given their difference in perimeter. The topological nature of the problem requires a careful choice of the solver to ensure convergence [47].

Figure 2(b) displays a real-space plot of $\mathrm{Im}\,Y_{\mathrm{ts}}$ as the tip is scanned across the sample, which reproduces clear peaks at the sample boundaries, $x = \pm 6\,\mu\mathrm{m}$. The spatial profile of these edge peaks, including the decay length inside the sample, agree quantitatively with the analytical predictions in Fig. 1(b). The most obvious difference lies in the asymmetry of $\mathrm{Im}\,Y_{\mathrm{ts}}$ inside and outside the sample in the simulation, which comes from the step and a change in dielectric environment across the sample boundary.

In Fig. 2(b), we note that the spatially resolved MIM signal is plotted at a series of generic frequencies, which are typically away from exact resonance frequencies. Upon analyzing the frequency dependence of $\mathrm{Im}Y_{\mathrm{ts}}$, we find the edge peak to be narrower at higher frequencies. This phenomenon has a

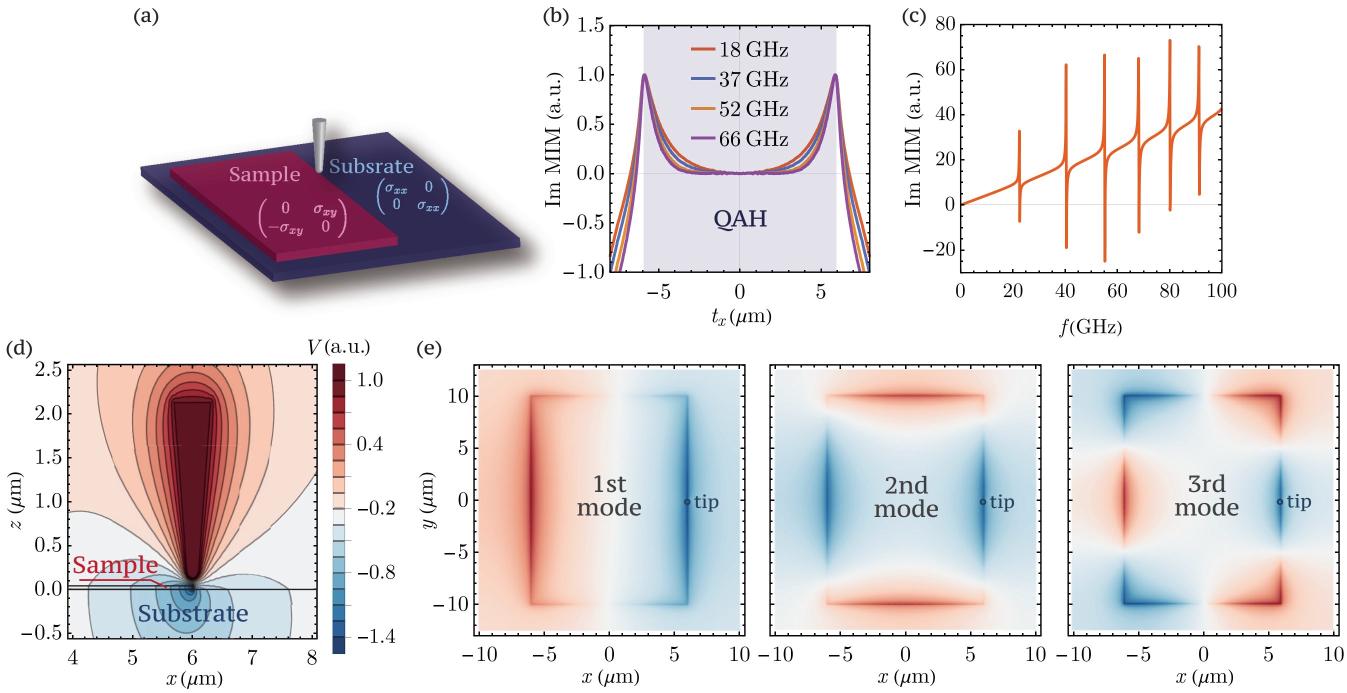

FIG. 2. Numerical simulation of topological edge magnetoplasmons in a QAH insulator. (a) Schematic illustration of the tip-sample setup used in the numerical simulation. The sample is characterized by the nonzero Hall conductance $\sigma_{xy} = e^2/h$ and the vanishing longitudinal conductance σ_{xx}. (b) Imaginary part of the MIM response, measured as a function of position across the sample, at various frequencies. A strong enhancement of the MIM response is observed at the sample boundaries due to the presence of edge magnetoplasmon (EMP) modes. (Note: Here we work with frequencies much higher than usually used in MIM experiments to compensate the fact that the EMP frequencies are scaled up when we scale down the sample dimension to ensure numerical convergence). (c) Imaginary part of the MIM response, plotted as a function of frequency when the tip is positioned over the sample edge. The difference between this simulation result and the analytical result in Fig. 1 mainly comes from the dielectric environment. (d), (e) Electric potential distribution in (d) the vertical plane across the tip and (e) the horizontal plane across the sample at the first few EMP resonances. The location of the tip is marked, which pins the phase of the edge charge distribution (see main text).

simple explanation within our theoretical framework. From Eq. (8), we know that a higher frequency ω corresponds to a larger EMP momentum k_ω. Meanwhile, $1/k_\omega$ sets the decay length scale of the MIM signal when the tip moves away from the edge [see Eq. (9)]. Combining these two observations, the peak is expected to be narrower at higher frequencies at which the MIM response comes from a higher-frequency EMP mode associated with a shorter decay length. This prediction is later compared with experiments in the following section.

When the tip is positioned over the sample edge, the imaginary part of Y_{ts} picks up a series of resonance peaks corresponding to the first few EMP modes [Fig. 2(c)], in agreement with analytical predictions. However, compared to Fig. 1(b), there is an additional contribution from the dielectric environment that scales linearly with the MIM frequency. Another noticeable feature is the absence of a zero frequency peak due to the factor of k_ω in Eq. (9). In Ref. [47] Sec. SIII B, we extract the dispersion of the EMP modes by identifying resonance peaks in $\mathrm{Im}\, Y_{\mathrm{ts}}$, which agrees quantitatively well with the classical part of Eq. (8).

Figures 2(d) and 2(e) illustrate the electric potential distribution in the plane of the sample at the first few EMP frequencies, which provides a visualization of the real-space charge density oscillations at the fundamental EMP mode and higher harmonics. As shown in Fig. 2(e), when the MIM frequency ω coincides with these EMP resonance frequencies, positive and negative charges start to concentrate at the sample edge with an in-plane distribution of $\delta n \sim \delta(r_\perp)e^{i(kr_\parallel+\phi)}$, where $r_\parallel$ is the distance along the edge and $r_\perp$ is the distance from the edge. We note that the phase ϕ is pinned by the location of the tip since the energy is minimized when the charge distribution is most negative beneath the tip. The characteristic potential distribution of standing wave patterns clearly identifies their plasmonic nature, while also confirming that the experimental setup is able to excite EMP modes. In Fig. 2(d), we see that the potential starts to decay immediately away from the edge, suggesting that charges are spatially confined to the boundaries of the sample.

Finally, we comment on the how expected MIM signatures of the EMP modes in a QAH insulator can be distinguished from the signatures of trivial edge modes arising from impurities at the boundaries of a conventional insulator. As shown in Ref. [47], Sec. SIV, the peak conductance required to reproduce the shape of the MIM curve is as high as 1×10^7 S/m, which would require a large concentration of metallic impurities that are extremely unlikely given the current fabrication process. Additionally, the peak in the MIM response at the boundaries of the sample is found to vanish at magnetic fields corresponding to the $\sigma_{xy} = 0$ phase, which suggests that the enhanced edge conduction is not trivial in nature [29]. Meanwhile, in the trivial case, the profile of the MIM edge peak would remain the same across a large range of frequencies,

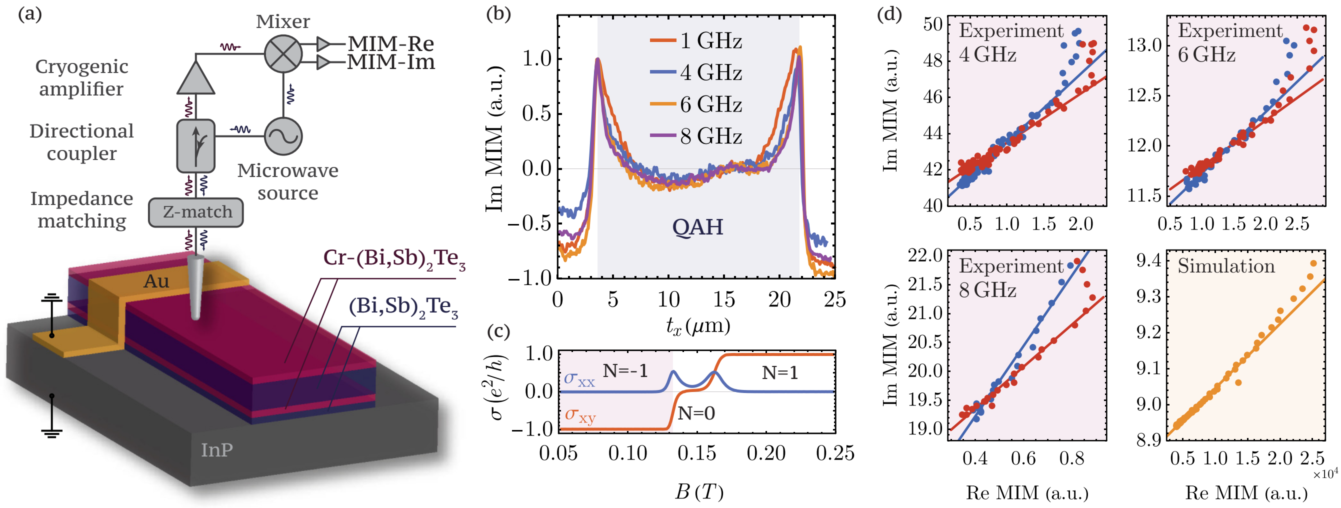

FIG. 3. Spatially resolved measurement of chiral edge states in a quantum anomalous Hall insulator. (a) Schematic illustration of the MIM experimental measurement setup. The tip is scanned across the sample, parallel to the shorter edge. (b) Experimental data reveal a strong enhancement of the imaginary part MIM response at the edge of the sample in the QAH regime (the sample lies within the shaded region). The measured edge peak profile becomes narrower as the MIM frequency increases. (c) Transport characterization of the sample, showing a well-quantized Hall conductance and vanishing longitudinal conductance in the QAH phase. (d) The Re MIM vs Im MIM scatter plot of the experimental data at 4, 6, and 8 GHz and the simulation results around the first EMP frequency. The red (blue) curves correspond to data close to the left (right) sample edge.

in contrast to the expected MIM response from EMP modes based on the theoretical picture presented above.

IV. EXPERIMENTAL RESULTS

To verify our theoretical framework, we performed real-space microwave imaging of one-dimensional QAH edge states in a high-quality magnetic topological insulator thin film at various frequencies. The experimental setup is shown in Fig. 3(a). The sample is a Cr-doped (Bi, Sb)$_2$Te$_3$ Hall bar with dimensions of 400 µm by 20 µm, and we scan the MIM tip across the device parallel to the short edge. Details on device preparation and the MIM measurement setup can be found in Ref. [47], Sec. SVI. Transport measurements are used for a baseline characterization of the quality of the QAH insulator state. As shown in Fig. 3(c), the Hall conductance σ_{xy} is fully quantized and the longitudinal conductance σ_{xx} drops to zero at $B = 50$ mT below the coercive field, suggesting that current is primarily transmitted by chiral edge modes that are topologically protected from backscattering in the QAH phases (labeled by Chern number $N = \pm 1$).

The presence of the QAH edge modes is manifested experimentally in a sharp enhancement of the MIM response at the boundaries of the sample, as shown in the spatially resolved microwave imaging data presented in Fig. 3(b). (We remind readers that the experiment and the numerical simulations were performed at very different frequencies to compensate the difference in sample dimensions, but the resulting MIM data can still be compared at a qualitative level).

These experimental results have a few surprising features that differ from the expected behavior of a conventional insulator with an enhanced edge conductivity with trivial origins. First of all, the observed MIM signal is much stronger than that expected from edge defects or local doping (see Ref. [47], Sec. SIV, for a comparison). If the MIM signal comes from the EMP modes, however, it is expected to diverge at EMP frequencies and can therefore be large in general. Another feature is that the real part of the measured MIM response is much smaller than the imaginary part, as shown in Fig. 3(d). This can be explained by Eq. (7) since Re $\chi(\boldsymbol{k})$ is tiny except when the MIM frequency precisely hits one of the EMP frequencies. In addition, the spatial profile of the MIM response near the sample edge becomes narrower at higher frequencies, which agrees qualitatively with the numerical simulations [see Figs. 3(b) and 2(b)].

Finally, we also investigate the relationship between the real and imaginary parts of the MIM response, measured as a function of position, at various frequencies. As shown in Fig. 3(d), we note that the real and imaginary parts of the observed MIM response have a linear relation at frequencies higher than 4 GHz. This linear relationship provides strong evidence in favor of EMP modes being responsible for the enhanced MIM signal at the sample edge and stands in sharp contrast to the expected semicircle relation predicted by the lumped-element model. The results suggest that the MIM signal mainly comes from a 1D edge, then the r dependence of ReMIM and ImMIM has to be the same. At frequencies lower than the first EMP resonance, the interpretation is complicated by the dielectric background. We refer interested readers to Ref. [47], Sec. SV, for more details.

V. DISCUSSION AND OUTLOOK

This paper provides the first quantitative interpretation of the MIM response of quantum materials within linear response theory. In the limit when the tip is sufficiently far from the sample, we show that the imaginary part of the MIM response can be quantitatively related to the electronic compressibility. We take this opportunity to compare MIM and the scanning single-electron transistor (SET) technique, which directly measures chemical potential and therefore the electronic compressibility [48,49]. MIM has the advantage of being less constrained by the electrostatic gating setup (and the associated fringing fields near the sample boundaries) and has a higher spatial resolution due to a simpler tip geometry, while scanning SET has the benefit of providing a more quantitative measurement of gap sizes and electronic compressibility without the need for impedance matching.

To illustrate a concrete application of the general model above, we compute the MIM response of a QAH insulator and reveal that the experimentally observed enhancement of the MIM signal at the sample boundaries comes from topological edge magnetoplasmon modes. This observation allows one to experimentally distinguish topologically nontrivial edge modes from trivial edge modes by investigating the quantitative relationship between the real and imaginary parts of the complex MIM response at multiple frequencies. Furthermore, this theoretical picture also allows us to predict the width $1/k_\omega$ of the experimentally observed peak of MIM response at the boundaries of Chern insulators, which explains the apparent inconsistencies between the edge-state decay length scales measured using MIM versus STM or transport [28,31,34–36].

To confirm and expand on the analytical results, we performed numerical simulations that took into account the effects of the tip-sample geometry and the dielectric background: the former turned out to be a small correction and the later only added linearly to the MIM signal. We also performed MIM measurements of the Chern insulator states in a Cr-doped $(\mathrm{Bi, Sb})_2\mathrm{Te}_3$ magnetic topological insulator at multiple GHz frequencies to verify our theoretical understanding. We observed a clear peak in the MIM response at the edge of the sample, whose spatial profile, frequency dependence, and ratio of the real and imaginary parts of the MIM signal were consistent with our framework. We would like to point out that future MIM experiments with continuous frequency tunability would be desirable to fully verify our EMP interpretation of the MIM edge response in QAH insulators.

We would also like to discuss how to measure the topological invariant of a Chern insulator using the technique of MIM. Expanding upon our previous calculations for QAH insulators with Chern number $\nu = 1$, the resonance frequency and MIM response can also be computed for systems with higher Chern numbers by including multiple branches in the density response calculation. At the classical level, we expect both the EMP frequencies and the MIM signal magnitude right on the resonance to be linearly proportional to the Chern number as shown in Fig. 4, $\hbar\omega_{\mathrm{EMP}} \propto C,\ \ Y_{\mathrm{ts}} \propto C$. We refer readers to Ref. [47] Eq. (S28) for the full analytical formula with quantum corrections. We also expect the lineshape of the MIM signal to depend on the dissipation along the chiral edge states (manifested in a finite σ_{xx}), as discussed in Sec. II. These features should allow the technique of MIM to shed light on the Chern number of a topological state, as well as the microscopic nature of the dissipation at the sample boundaries.

Finally, we want to emphasize that our theoretical framework is suitable for arbitrary quantum materials though we focus on QAH insulators in this work as an illustration. The only assumption used in the derivation is the microwave being weak enough to remain in the linear response regime, which is always true in the MIM setup. The geometry of the tip is captured by the Coulomb interaction $G(\mathbf{r}, \mathbf{r}')$, which can be accurately obtained from a finite element calculation. In the future, we will exploit the power of this framework to study more exotic quantum materials including strange metals, topological superconductors, and fractional quantum Hall insulators.

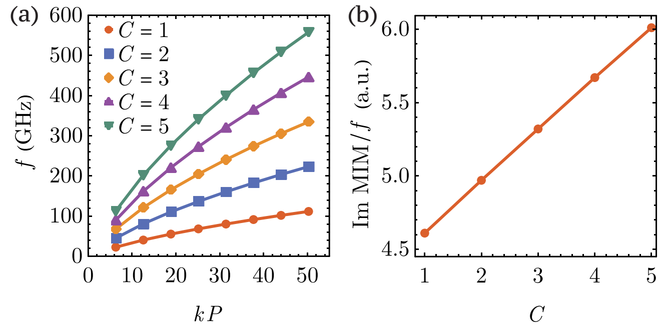

FIG. 4. Numerically simulated MIM response of a higher Chern number insulator. Here we present numerical simulations of the MIM response of a Chern insulator with the tip positioned directly over the edge state. The topological invariant, or Chern number, is C. (a) Plot of the EMP resonance frequencies for a variety of Chern insulator states with different integers C. The curves can be fitted by the same parameters of ϵ_r and l as in the inset of Fig. 2(c). (b) Imaginary part of the MIM signal at the EMP frequency f, plotted as a function of the Chern number. Here we consider a finite dissipation $\sigma_{xx} \neq 0$ and factor out the trivial factor f in Eq. (2) for clarity. The MIM signal has a finite magnitude at $C = 0$ due to baseline contributions from the dielectric environment.

ACKNOWLEDGMENTS

We thank Allan H. MacDonald, Tarun Grover, Yongtao Cui, Rahul Roy, Massoud R. Masir, Yahya Alavirad, and Adrian B. Culver for inspiring discussions. We thank Alex Cauchon for helping develop some of the numerical simulations. M.T.A acknowledges funding support from the UC Office of the President, specifically the UC Laboratory Fees Research Program (Award No. LFR-20-653926) and the AFOSR Young Investigator Program (Award No. FA9550-20-1-0035). T.W. is supported by the U.S. Department of Energy, Office of Science, Office of Basic Energy Sciences, Materials Sciences and Engineering Division, under Contract No. DE-AC02-05-CH11231 (van der Waals Heterostructures Program KCWF16). This work was partly supported by Japan Science and Technology Agency Core Research for Evolutional Science and Technology (Grant No. JPMJCR16F1). Y.-Z.Y. is supported by the NSF through (Grant No. DMR-2238360). Microwave impedance microscopy measurements at Stanford University were supported by the Gordon and Betty Moore Foundation's Emergent Phenomena in Quantum Systems initiative through Grant No. GBMF4546 (Z.-X.S.) and by the National Science Foundation through (Grant No. DMR-1305731).

[1] K. von Klitzing, Quantum Hall effect: Discovery and application, Annu. Rev. Condens. Matter Phys. **8**, 13 (2017).
[2] C. Dean, P. Kim, J. I. A. Li, and A. Young, Fractional quantum Hall effects in graphene, in *Fractional Quantum Hall Effects*, edited by B. I. Halperin and J. K. Jain (World Scientific, Singapore, 2020), Chap. 7, pp. 317–375.
[3] C.-X. Liu, S.-C. Zhang, and X.-L. Qi, The quantum anomalous Hall effect: Theory and experiment, Annu. Rev. Condens. Matter Phys. **7**, 301 (2016).
[4] K. He, Y. Wang, and Q.-K. Xue, Topological materials: Quantum anomalous Hall system, Annu. Rev. Condens. Matter Phys. **9**, 329 (2018).
[5] Y. Deng, Y. Yu, M. Z. Shi, Z. Guo, Z. Xu, J. Wang, X. H. Chen, and Y. Zhang, Quantum anomalous Hall effect in intrinsic magnetic topological insulator $MnBi_2Te_4$, Science **367**, 895 (2020).
[6] A. L. Sharpe, E. J. Fox, A. W. Barnard, J. Finney, K. Watanabe, T. Taniguchi, M. A. Kastner, and D. Goldhaber-Gordon, Emergent ferromagnetism near three-quarters filling in twisted bilayer graphene, Science **365**, 605 (2019).
[7] M. Serlin, C. L. Tschirhart, H. Polshyn, Y. Zhang, J. Zhu, K. Watanabe, T. Taniguchi, L. Balents, and A. F. Young, Intrinsic quantized anomalous Hall effect in a moiré heterostructure, Science **367**, 900 (2020).
[8] M. He, Y.-H. Zhang, Y. Li, Z. Fei, K. Watanabe, T. Taniguchi, X. Xu, and M. Yankowitz, Competing correlated states and abundant orbital magnetism in twisted monolayer-bilayer graphene, Nat. Commun. **12**, 4727 (2021).
[9] G. Chen, A. L. Sharpe, E. J. Fox, Y.-H. Zhang, S. Wang, L. Jiang, B. Lyu, H. Li, K. Watanabe, T. Taniguchi, Z. Shi, T. Senthil, D. Goldhaber-Gordon, Y. Zhang, and F. Wang, Tunable correlated Chern insulator and ferromagnetism in a moiré superlattice, Nature (London) **579**, 56 (2020).
[10] L. Wang, E.-M. Shih, A. Ghiotto, L. Xian, D. A. Rhodes, C. Tan, M. Claassen, D. M. Kennes, Y. Bai, B. Kim, K. Watanabe, T. Taniguchi, X. Zhu, J. Hone, A. Rubio, A. N. Pasupathy, and C. R. Dean, Correlated electronic phases in twisted bilayer transition metal dichalcogenides, Nat. Mater. **19**, 861 (2020).
[11] L. P. Kouwenhoven, B. J. van Wees, N. C. van der Vaart, C. J. P. M. Harmans, C. E. Timmering, and C. T. Foxon, Selective population and detection of edge channels in the fractional quantum Hall regime, Phys. Rev. Lett. **64**, 685 (1990).
[12] B. J. van Wees, E. M. M. Willems, C. J. P. M. Harmans, C. W. J. Beenakker, H. van Houten, J. G. Williamson, C. T. Foxon, and J. J. Harris, Anomalous integer quantum Hall effect in the ballistic regime with quantum point contacts, Phys. Rev. Lett. **62**, 1181 (1989).
[13] M. Büttiker, Absence of backscattering in the quantum Hall effect in multiprobe conductors, Phys. Rev. B **38**, 9375 (1988).
[14] R. Sabo, I. Gurman, A. Rosenblatt, F. Lafont, D. Banitt, J. Park, M. Heiblum, Y. Gefen, V. Umansky, and D. Mahalu, Edge reconstruction in fractional quantum Hall states, Nat. Phys. **13**, 491 (2017).
[15] S. Howard, L. Jiao, Z. Wang, N. Morali, R. Batabyal, P. Kumar-Nag, N. Avraham, H. Beidenkopf, P. Vir, E. Liu, C. Shekhar, C. Felser, T. Hughes, and V. Madhavan, Evidence for one-dimensional chiral edge states in a magnetic Weyl semimetal $Co_3Sn_2S_2$, Nat. Commun. **12**, 4269 (2021).
[16] H.-K. Xu, M. Gu, F. Fei, Y.-S. Gu, D. Liu, Q.-Y. Yu, S.-S. Xue, X.-H. Ning, B. Chen, H. Xie, Z. Zhu, D. Guan, S. Wang, Y. Li, C. Liu, Q. Liu, F. Song, H. Zheng, and J. Jia, Observation of magnetism-induced topological edge state in antiferromagnetic topological insulator $MnBi_4Te_7$, ACS Nano **16**, 9810 (2022).
[17] F. Lüpke, A. D. Pham, Y.-F. Zhao, L.-J. Zhou, W. Lu, E. Briggs, J. Bernholc, M. Kolmer, J. Teeter, W. Ko, C.-Z. Chang, P. Ganesh, and A.-P. Li, Local manifestations of thickness-dependent topology and edge states in the topological magnet $MnBi_2Te_4$, Phys. Rev. B **105**, 035423 (2022).
[18] C. Zhang, T. Zhu, S. Kahn, T. Soejima, K. Watanabe, T. Taniguchi, A. Zettl, F. Wang, M. P. Zaletel, and M. F. Crommie, Visualizing and manipulating chiral edge states in a moiré quantum anomalous Hall insulator, arXiv:2212.03380.
[19] S. Tang, C. Zhang, D. Wong, Z. Pedramrazi, H.-Z. Tsai, C. Jia, B. Moritz, M. Claassen, H. Ryu, S. Kahn, J. Jiang, H. Yan, M. Hashimoto, D. Lu, R. G. Moore, C.-C. Hwang, C. Hwang, Z. Hussain, Y. Chen, M. M. Ugeda *et al.*, Quantum spin Hall state in monolayer 1T'-WTe_2, Nat. Phys. **13**, 683 (2017).
[20] E. M. Spanton, K. C. Nowack, L. Du, G. Sullivan, R.-R. Du, and K. A. Moler, Images of edge current in InAs/GaSb quantum wells, Phys. Rev. Lett. **113**, 026804 (2014).
[21] F. Nichele, H. J. Suominen, M. Kjaergaard, C. M. Marcus, E. Sajadi, J. A. Folk, F. Qu, A. J. A. Beukman, F. K. de Vries, and J. van Veen, Edge transport in the trivial phase of InAs/GaSb, New J. Phys. **18**, 083005 (2016).
[22] K. C. Nowack, E. M. Spanton, M. Baenninger, M. König, J. R. Kirtley, G. Kalisky, C. Ames, P. Leubner, C. Brüne, H. Buhmann, L. W. Molenkamp, D. Goldhaber-Gordon, and K. A. Moler, Imaging currents in HgTe quantum wells in the quantum spin Hall regime, Nat. Mater. **12**, 787 (2013).
[23] M. T. Allen, O. Shtanko, I. C. Fulga, A. R. Akhmerov, K. Watanabe, T. Taniguchi, P. Jarillo-Herrero, L. S. Levitov, and A. Yacoby, Spatially resolved edge currents and guided-wave electronic states in graphene, Nat. Phys. **12**, 128 (2016).
[24] E. Y. Ma, M. R. Calvo, J. Wang, B. Lian, M. Mühlbauer, C. Brüne, Y.-T. Cui, K. Lai, W. Kundhikanjana, Y. Yang, M. Baenninger, M. König, C. Ames, H. Buhmann, P. Leubner, L. W. Molenkamp, S.-C. Zhang, D. Goldhaber-Gordon, M. A. Kelly, and Z.-X. Shen, Unexpected edge conduction in mercury telluride quantum wells under broken time-reversal symmetry, Nat. Commun. **6**, 7252 (2015).
[25] C.-Z. Chang, W. Zhao, D. Y. Kim, P. Wei, J. K. Jain, C. Liu, M. H. W. Chan, and J. S. Moodera, Zero-field dissipationless chiral edge transport and the nature of dissipation in the quantum anomalous Hall state, Phys. Rev. Lett. **115**, 057206 (2015).
[26] X. Kou, S.-T. Guo, Y. Fan, L. Pan, M. Lang, Y. Jiang, Q. Shao, T. Nie, K. Murata, J. Tang, Y. Wang, L. He, T.-K. Lee, W.-L. Lee, and K. L. Wang, Scale-invariant quantum anomalous Hall effect in magnetic topological insulators beyond the two-dimensional limit, Phys. Rev. Lett. **113**, 137201 (2014).
[27] Y. Shi, J. Kahn, B. Niu, Z. Fei, B. Sun, X. Cai, B. A. Francisco, D. Wu, Z.-X. Shen, X. Xu, D. H. Cobden, and Y.-T. Cui, Imaging quantum spin Hall edges in monolayer WTe_2, Sci. Adv. **5**, eaat8799 (2019).
[28] K. Lai, W. Kundhikanjana, M. A. Kelly, Z.-X. Shen, J. Shabani, and M. Shayegan, Imaging of Coulomb-driven quantum Hall edge states, Phys. Rev. Lett. **107**, 176809 (2011).
[29] M. Allen, Y. Cui, E. Yue Ma, M. Mogi, M. Kawamura, I. C. Fulga, D. Goldhaber-Gordon, Y. Tokura, and Z.-X. Shen, Visualization of an axion insulating state at the transition between 2 chiral quantum anomalous Hall states, Proc. Natl. Acad. Sci. USA **116**, 14511 (2019).

[30] W. Lin, Y. Feng, Y. Wang, J. Zhu, Z. Lian, H. Zhang, H. Li, Y. Wu, C. Liu, Y. Wang, J. Zhang, Y. Wang, C.-Z. Chen, X. Zhou, and J. Shen, Direct visualization of edge state in even-layer $MnBi_2Te_4$ at zero magnetic field, Nat. Commun. **13**, 7714 (2022).

[31] Y.-T. Cui, B. Wen, E. Y. Ma, G. Diankov, Z. Han, F. Amet, T. Taniguchi, K. Watanabe, D. Goldhaber-Gordon, C. R. Dean, and Z.-X. Shen, Unconventional correlation between quantum Hall transport quantization and bulk state filling in gated graphene devices, Phys. Rev. Lett. **117**, 186601 (2016).

[32] G. Qiu, P. Zhang, P. Deng, S. K. Chong, L. Tai, C. Eckberg, and K. L. Wang, Mesoscopic transport of quantum anomalous Hall effect in the submicron size regime, Phys. Rev. Lett. **128**, 217704 (2022).

[33] L.-J. Zhou, R. Mei, Y.-F. Zhao, R. Zhang, D. Zhuo, Z.-J. Yan, W. Yuan, M. Kayyalha, M. H. W. Chan, C.-X. Liu, and C.-Z. Chang, Confinement-induced chiral edge channel interaction in quantum anomalous Hall insulators, Phys. Rev. Lett. **130**, 086201 (2023).

[34] H. Hettmansperger, F. Duerr, J. B. Oostinga, C. Gould, B. Trauzettel, and L. W. Molenkamp, Quantum Hall effect in narrow graphene ribbons, Phys. Rev. B **86**, 195417 (2012).

[35] S. Kim, J. Schwenk, D. Walkup, Y. Zeng, F. Ghahari, S. T. Le, M. R. Slot, J. Berwanger, S. R. Blankenship, K. Watanabe, T. Taniguchi, F. J. Giessibl, N. B. Zhitenev, C. R. Dean, and J. A. Stroscio, Edge channels of broken-symmetry quantum Hall states in graphene visualized by atomic force microscopy, Nat. Commun. **12**, 2852 (2021).

[36] T. Johnsen, C. Schattauer, S. Samaddar, A. Weston, M. J. Hamer, K. Watanabe, T. Taniguchi, R. Gorbachev, F. Libisch, and M. Morgenstern, Mapping quantum Hall edge states in graphene by scanning tunneling microscopy, Phys. Rev. B **107**, 115426 (2023).

[37] M. Wassermeier, J. Oshinowo, J. P. Kotthaus, A. H. MacDonald, C. T. Foxon, and J. J. Harris, Edge magnetoplasmons in the fractional-quantum-Hall-effect regime, Phys. Rev. B **41**, 10287(R) (1990).

[38] E. Y. Andrei, D. C. Glattli, F. I. B. Williams, and M. Heiblum, Low frequency collective excitations in the quantum-Hall system, Surf. Sci. **196**, 501 (1988).

[39] N. Kumada, P. Roulleau, B. Roche, M. Hashisaka, H. Hibino, I. Petković, and D. C. Glattli, Resonant edge magnetoplasmons and their decay in graphene, Phys. Rev. Lett. **113**, 266601 (2014).

[40] A. C. Mahoney, J. I. Colless, L. Peeters, S. J. Pauka, E. J. Fox, X. Kou, L. Pan, K. L. Wang, D. Goldhaber-Gordon, and D. J. Reilly, Zero-field edge plasmons in a magnetic topological insulator, Nat. Commun. **8**, 1836 (2017).

[41] V. A. Volkov and S. A. Mikhailov, Edge magnetoplasmons: Low frequency weakly damped excitations in inhomogeneous two-dimensional electron systems, Zh. Eksp. Teor. Fiz. **94**, 217 (1988) [Sov. Phys. JETP **67**, 1639 (1988)].

[42] J. C. W. Song and M. S. Rudner, Chiral plasmons without magnetic field, Proc. Natl. Acad. Sci. USA **113**, 4658 (2016).

[43] D. Jin, L. Lu, Z. Wang, C. Fang, J. D. Joannopoulos, M. Soljačić, L. Fu, and N. X. Fang, Topological magnetoplasmon, Nat. Commun. **7**, 13486 (2016).

[44] J. Cano, A. C. Doherty, C. Nayak, and D. J. Reilly, Microwave absorption by a mesoscopic quantum Hall droplet, Phys. Rev. B **88**, 165305 (2013).

[45] E. Y. Ma, Emerging electronic states at boundaries and domain walls in quantum materials, Ph.D. thesis, Stanford University (2016).

[46] M. E. Barber, E. Y. Ma, and Z.-X. Shen, Microwave impedance microscopy and its application to quantum materials, Nat. Rev. Phys. **4**, 61 (2022).

[47] See Supplemental Material at http://link.aps.org/supplemental/10.1103/PhysRevB.108.235432 for the methods used in the analytical derivation, the numerical simulation, and the experiment [54–59]. It also provides comparison of the general framework and the lumped-element model; and comparison of the topological edge states and the trivial edge states.

[48] J. Yu, B. A. Foutty, Z. Han, M. E. Barber, Y. Schattner, K. Watanabe, T. Taniguchi, P. Phillips, Z.-X. Shen, S. A. Kivelson, and B. E. Feldman, Correlated Hofstadter spectrum and flavour phase diagram in magic-angle twisted bilayer graphene, Nat. Phys. **18**, 825 (2022).

[49] J. Yu, B. A. Foutty, Y. H. Kwan, M. E. Barber, K. Watanabe, T. Taniguchi, Z.-X. Shen, S. A. Parameswaran, and B. E. Feldman, Spin skyrmion gaps as signatures of strong-coupling insulators in magic-angle twisted bilayer graphene, Nat. Commun. **14**, 6679 (2023).

[50] A. M. Chang, Chiral Luttinger liquids at the fractional quantum Hall edge, Rev. Mod. Phys. **75**, 1449 (2003).

[51] A. Gourmelon, H. Kamata, J.-M. Berroir, G. Fève, B. Plaçais, and E. Bocquillon, Characterization of helical Luttinger liquids in microwave stepped-impedance edge resonators, Phys. Rev. Res. **2**, 043383 (2020).

[52] I. L. Aleiner and L. I. Glazman, Novel edge excitations of two-dimensional electron liquid in a magnetic field, Phys. Rev. Lett. **72**, 2935 (1994).

[53] S. Conti and G. Vignale, Collective modes and electronic spectral function in smooth edges of quantum Hall systems, Phys. Rev. B **54**, R14309(R) (1996).

[54] X.-G. Wen, Theory of the edge states in fractional quantum Hall effects, Int. J. Mod. Phys. B **06**, 1711 (1992).

[55] X. G. Wen, Gapless boundary excitations in the quantum Hall states and in the chiral spin states, Phys. Rev. B **43**, 11025 (1991).

[56] Z. D. Shi, H. Goldman, D. V. Else, and T. Senthil, Gifts from anomalies: Exact results for Landau phase transitions in metals, SciPost Phys. **13**, 102 (2022).

[57] T. Morinari and N. Nagaosa, Edge modes in the hierarchical fractional quantum Hall liquids with Coulomb interaction, Solid State Commun. **100**, 163 (1996).

[58] M. Mogi, R. Yoshimi, A. Tsukazaki, K. Yasuda, Y. Kozuka, K. S. Takahashi, M. Kawasaki, and Y. Tokura, Magnetic modulation doping in topological insulators toward higher-temperature quantum anomalous Hall effect, Appl. Phys. Lett. **107**, 182401 (2015).

[59] Y.-T. Cui, E. Y. Ma, and Z.-X. Shen, Quartz tuning fork based microwave impedance microscopy, Rev. Sci. Instrum. **87**, 063711 (2016).